Merged Magnetic Resonance and Light Sheet Microscopy of the Whole Mouse Brain

Supplemental Information

Experiment 1 Reference Framework		Strain: C57BL/6J						
Specimen	Sex	Volume (mm^3)	Spatial Res (μm)	Angular Res	Time (hrs)	MGRE	Data (GB)	Light Sheet
191209-1:1	M	534	15	108	245	Yes	252	NeuN/Syto16/MBP
200302-1:1	M	561	15	108	245	Yes	252	NeuN/MBP/AutoF
200316-1:1	F	509	15	108	245	Yes	252	NeuN/MBP/AutoF

Experiment 2 Resolution		Strain: B6.Cg-Tg (Thy1-YFG)HJrs/J						
Specimen	Sex	Volume (mm^3)	Spatial Res (μm)	Angular Res	Time (hrs)	MGRE	Data (GB)	Light Sheet
190415-2:1	M	503	15	61	135	No	84	Thy1-YFG/AutoF
190415-1:1	M	560	25	108	126	No	51	Thy1-YFG/AutoF
190415-4:1	M	556	25	61	60	No	25	Thy1-YFG/AutoF

Experiment 3 Hi Res Aging		Strain: BXD89							
Specimen	Sex	Volume (mm^3)	Age (days)	Spatial Res (μm)	Angular Res	Time (hrs)	MGRE	Data (GB)	Light Sheet
190108-5:1	M	457	111	15	108	245	Yes	252	NeuN/ Syto16/ibai1
200803-12:1	M	524	687	15	108	245	Yes	252	NeuN /Syto16/ibai1

Experiment 4 Hi Throughput Aging		Strains: BXD 24, 29, 34, 43, 44, 48a, 51 60, 62, 65b, 77, 89,101						
Group	Gender/ Number	Mean Age (days)	Age Range	Spatial Res (μm)	Angular Res	Time (hrs)	MGRE	Data (MB)
Young	M/ 22 F/ 25	102	72/176	45	46	11.8	Yes	220
Old	M/ 30 F/ 34	463	341/687	45	46	11.8	Yes	220

Table S1. *Details of specimens and acquisition protocols for four different HiDiver experiments*

Specimen Preparation. All procedures were approved by the Duke University institution animal care and use committee. Four groups of animals were studied (**Table S1**). Experiment 1: Adult male and female C57BL/6J mice were purchased from The Jackson Laboratory (JAX) to create the HiDiver atlases. Experiment 2: Adult male and female B6.Cg-Tg (Thy1-YFG/HJrs/J) mice were purchased from JAX to validate tractography. Experiment 3: A young (111 day) male BXD89 mouse and an old (687 day) male BXD 89 mouse were obtained from the University of Tennessee Health Science Center to demonstrate the application of the methods to our primary focus—the neurogenetics of aging at the highest spatial resolution. Experiment 4: A total of 111 animals in 13 of the BXD strains were obtained from the University of Tennessee Health Science Center to demonstrate the application of the methods in a high throughput study. All animals

were allowed to adjust to their new environment for one week or more. All animals were perfused with 10% Prohance (Gadoteridol) in buffered formalin [1] [2]. Prohance is a chelated gadolinium compound commonly used in clinical MRI as a contrast agent. It is used as an active stain in MRH to reduce the spin-lattice relaxation time (T1) from 1800 to 100 ms [1]. Animals were anesthetized to a surgical plane with pentobarbital. A 21-gauge needle connected to a peristaltic pump was inserted in the left ventricle. Blood was flushed using a 0.1% heparin saline solution, followed by perfusion with the Prohance/formalin mixture for ~ 6 min. Heads were placed in buffered formalin for an additional 24 h. Mandibles were removed and skin and muscle removed to allow use of a smaller radiofrequency coil, and brains in the cranium were placed in an 0.5% Prohance/buffer solution.

MRH Scalar Volumes. The four echoes of the MGRE image were averaged together to generate an (AvgMGRE) image. A pipeline registered the 3D volumes to correct for eddy current distortions. It starts with a skull stripping algorithm [3]. The ANTs pipeline uses linear scaling and affine transforms to produce the average baseline image. The individual diffusion weighted volumes were then registered to $Avgb_0$ producing a 4D array of the registered 3D volumes using our SAMBA pipeline [4] [5]. A MATLAB script averaged all the diffusion weighted 3D volumes to produce the diffusion weighted image (DWI). The 4D denoised volume was passed to DSI Studio (http://dsi-studio.labsolver.org/) where a Perl script executed an initial pass using the diffusion tensor algorithm [6] to generate five different 3D scalar volumes: 1) axial diffusivity (AD); 2) radial diffusivity (RD); 3) mean diffusivity (MD); 4) fractional anisotropy (FA); and 5) the color fractional anisotropy (clrFA) images. These six 3D scalar images have decidedly different contrasts and highlight different anatomical features, boundaries, and orientations of cellular components (**Figure 1**). The DWI and FA images were used to drive the registration of the atlas and associated labels.

Source Data	Algorithm	Name	Abbreviation
MGRE	Average	Average	AvgMGRE
DTI	ANTs	Average Baseline	$Avgb_0$
	Average	Diffusion Weighted Image	DWI
	DTI	Mean Diffusivity	MD
		Axial Diffusivity	AD
		Radial Diffusivity	RB
		Fractional Anisotropy	FA
		Color Fractional Anisotropy	ClrFA
DTI	GQI	Isotropic Fraction	iso
		Normalized Quantitative Anisotropy	nqa
	Calamante	Track Density Imaging	TDI
		Color Track Density Imaging	ClrTDI

***Table S2**. Summary of different contrast volumes generated in the standard HiDiver/MRH protocol including the algorithms used and the abbreviations*

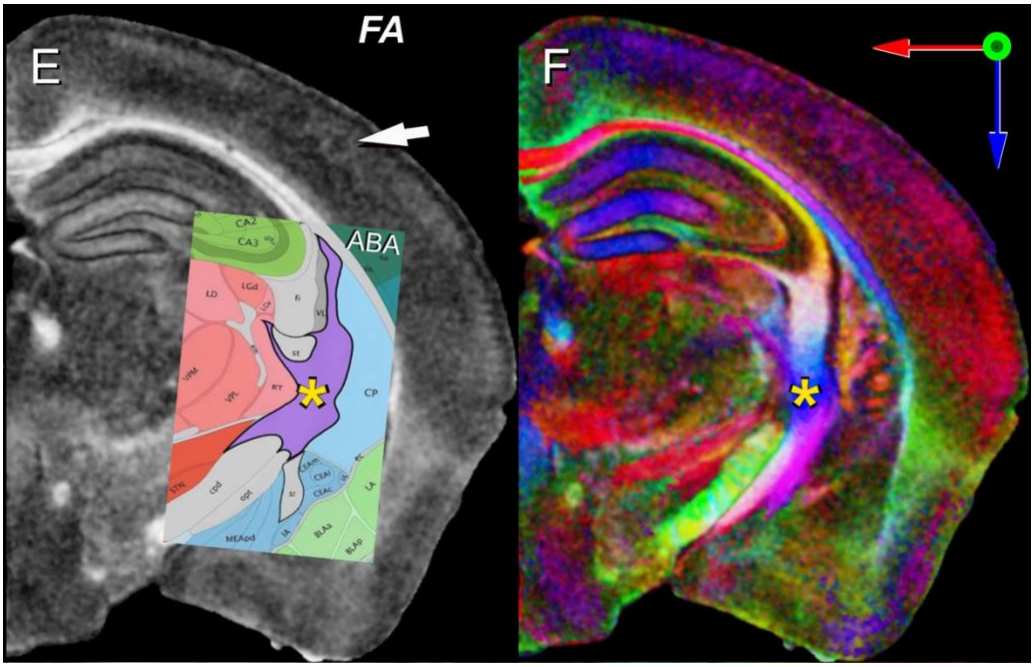

***Figure S1.** This is an extension of Figure 1. **Panel E** displays the fractional anisotropy where image intensity reflects the anisotropic diffusion in each voxel**.** The overlay in panel **E** is from the Allen Brain Atlas CCFv3 [7].**Panel F** adds color in which the primary axis of diffusion is encoded in color. It is straightforward in the color FA to define all tracts disambiguated in CCFv3.*

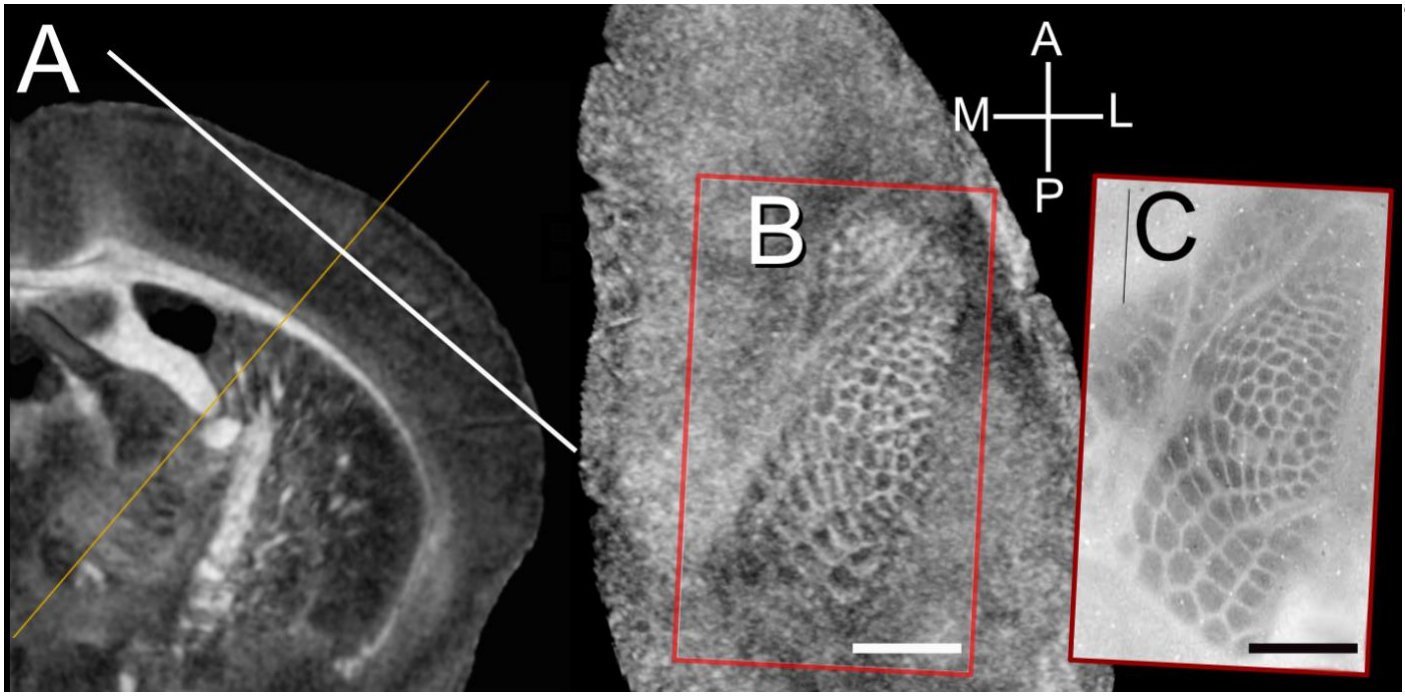

Fig S2. Barrel cortex digital flatmount of a C57BL/6J *(Specimen 200302-1:1).* ***A.*** *Coronal FA section in which the orientation of the tangential plane through layer 4 of the barrel field is highlighted by a long white two-headed arrow.* ***B.*** *A single 15-µm-thick FA oblique slice of the left cortex in a plane tangential to the barrel field. The white calibration bars are 1 mm. In* ***C*** *we have juxtaposed an image of a cortical flatmount from the same strain taken from [8] (their figure 1B with its own thin black 1 mm calibration bar). The alignment is remarkably precise with only linear rescaling.*

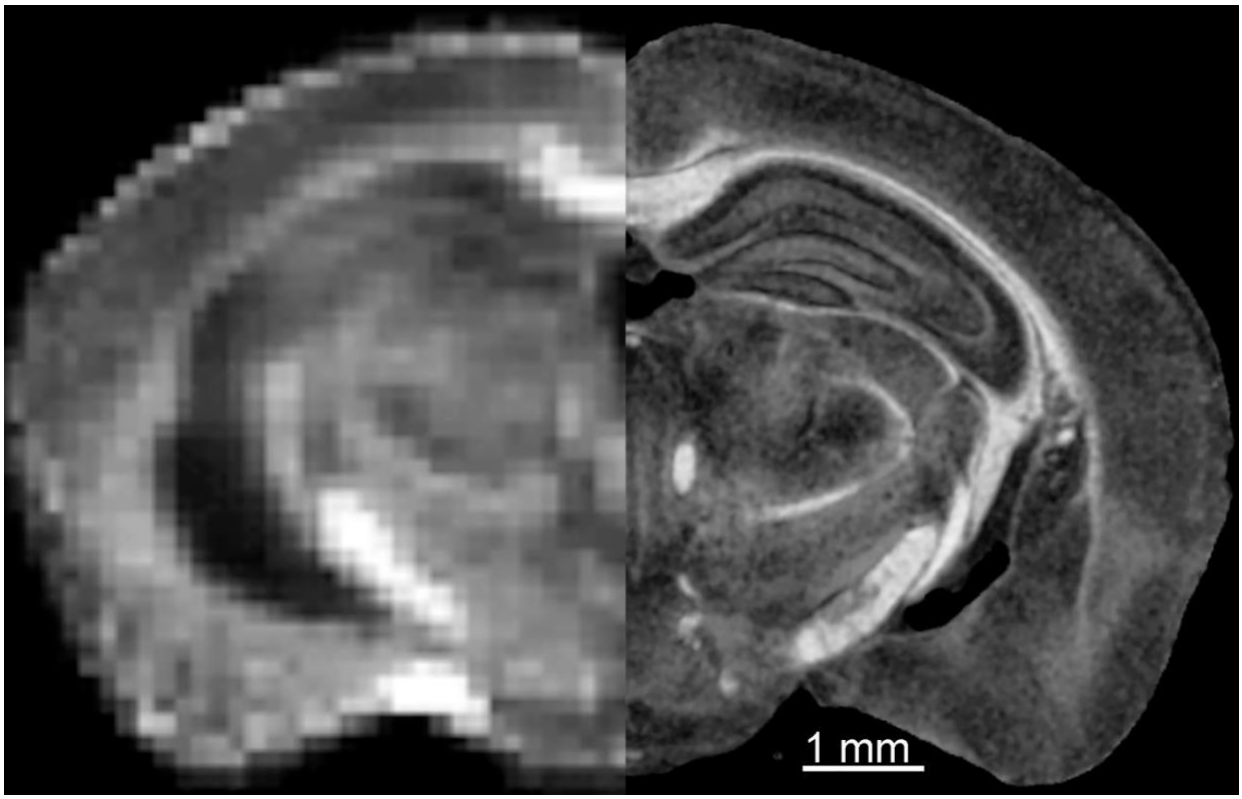

Figure S3. *Comparison in vivo fractional anisotropy image @ 150* μm^3 *(left) with ex vivo MR histology fractional anisotropy image @ 15* μm^3 *(right). In vivo image Courtesy of Professor Ian Shih, University of North Carolina (https://www.med.unc.edu/bric/camri/imaging-service/mouse-brain-in-vivo-epi-dti/)*

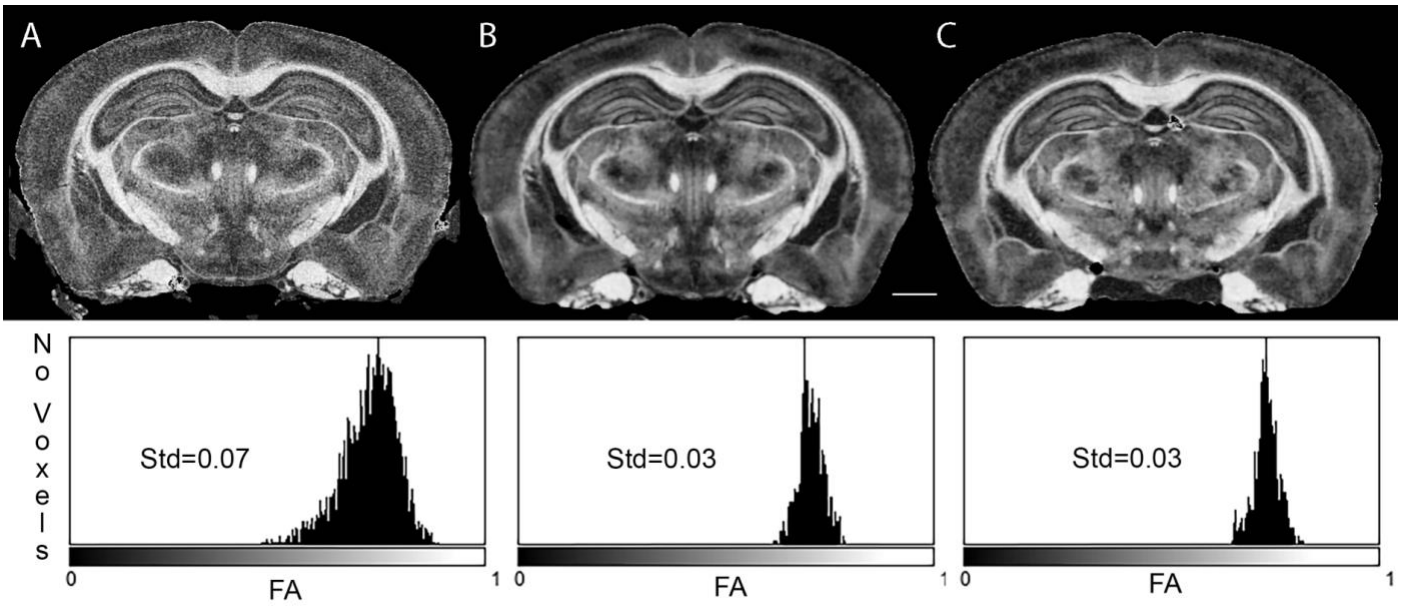

Figure S4. *Comparison of spatial and angular resolution A) Specimen 190415-2:1: 15* μm, *61 angles; B) 190415-1:1 25* μm, *108 angles; C) 25*μm, *61 angles. Histograms of a ROI in corpus callosum show changes in precision in calculating FA. Scale bar is 1 mm.*

Denoising. St-Jean and colleagues have developed a novel denoising algorithm that exploits the fourth (angular) dimension of the data [9]. The volume is decomposed into 4D overlapping patches that sample both the spatial and angular resolution. A dictionary of atoms is learned on the patches and a sparse decomposition is generated by bounding the reconstruction error with the local noise variance. The method improved the visibility of structures while simultaneously reducing the number of spurious tracts. St-Jean and colleagues implemented the algorithm for high resolution clinical scans (matrix of 210x210x210) of ~ 20 MB/volume with 40 volumes (~800 MB). The atlases generated for this work were acquired with arrays as large 800x800x1600 with 108 angular samples plus 13 baseline images—a 4D volume that is more than 300 times larger (~252 GB).To accommodate the change of scale, the algorithm was implemented on the cluster (**Figure S14**) by breaking the volume into overlapping cubes that could be processed in parallel**.**

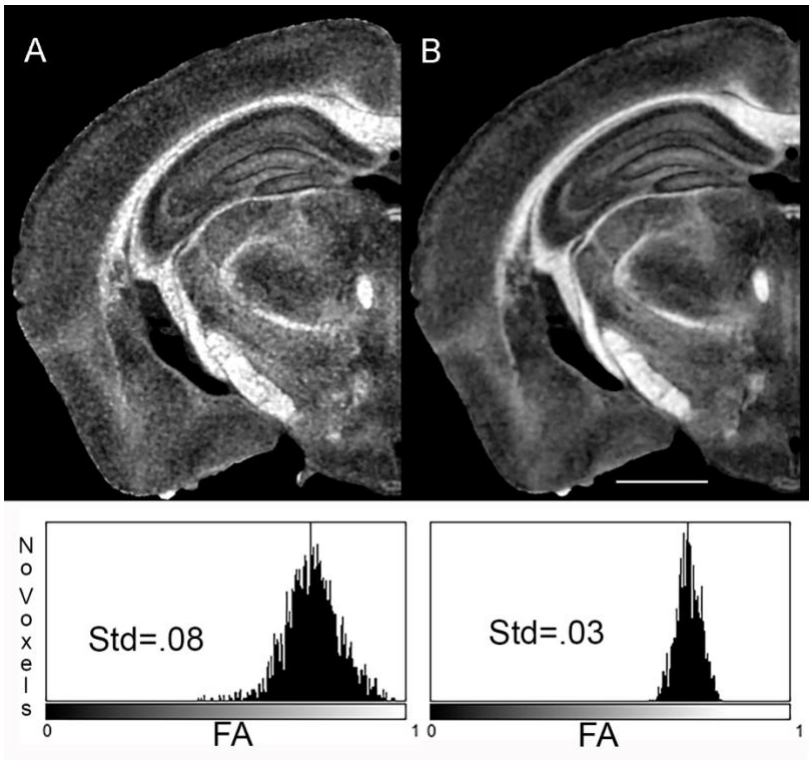

Figure S5. *Specimen 200316-1:1(Table 1) @ 15* μm, isotopic spatial resolution A) before denoising; B) after denoising. *Histograms of a ROI in corpus callosum show changes in precision in calculating FA. Scale bar is 1 mm*

Figure S6. *Representative A) DWI and B) QA images from higher throughput (20 hr) 25* μm, *61 angle acquisition. Scan time has been reduced using a fast spin echo that acquired two lines of K space per TR.* The scale bar is 1 mm

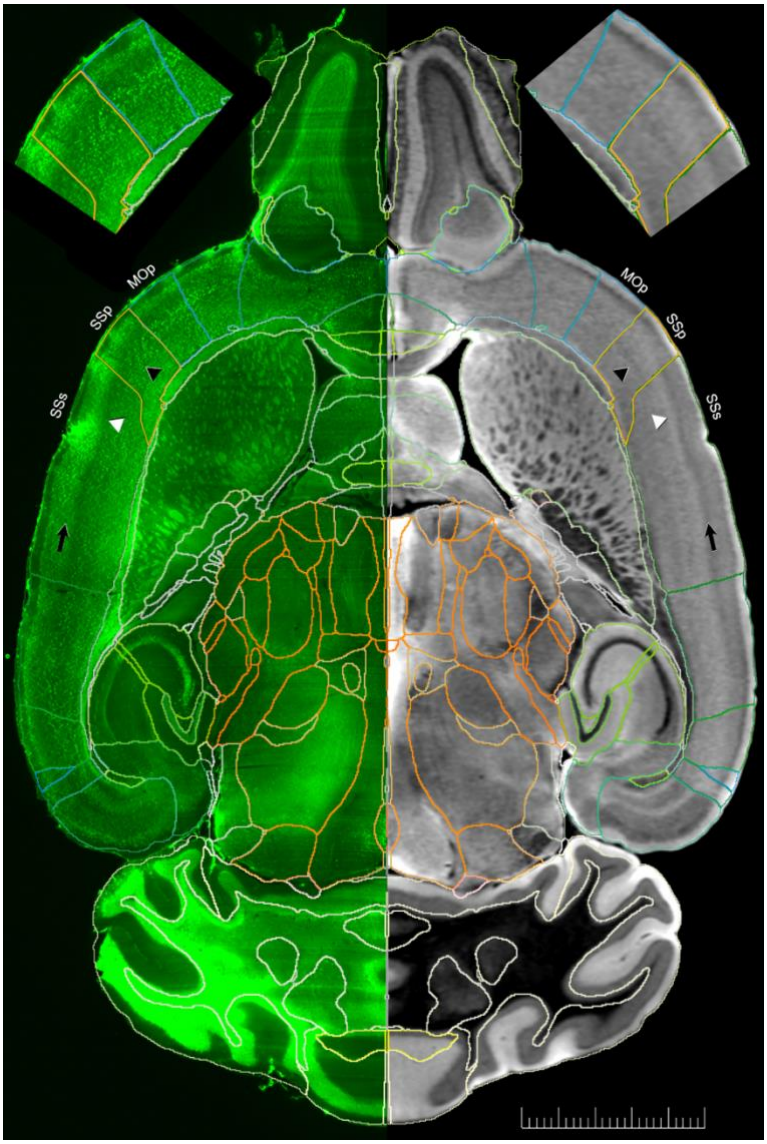

Figure S7 Accurate transfer of ROIs across age and genotype. *NeuN (**left**) and axial DWI (**right**); images are from an old BXD89 male (687 days, specimen* 200803-12:1*, also see **Fig 6B** and **D**). ROIs were lifted over from the C57BL/6J reference volume to the MRH using the SAMBA pipeline. ROIs were then transferred to the NeuN LSM channel using a second registration pipeline also built on ANTs. The final ROIs have been integrated into all three channels of the LSM at full resolution LSM (1.8 x 1.8 x 4.0 µm). Three cortical areas are marked—the primary motor area (**MOp**), the primary somatosensory area (**SSp**), and the supplemental (secondary) somatosensory area (**SSs**). The **insets** are 1.5X magnifications of these three areas. While LSM has higher resolution, the MRH DWI modality highlights cytoarchitectonic boundaries more prominently. The dark DWI band (**arrows**) in SSs is layer 4 whereas the adjacent light band is layer 5a (**white triangles**). In SSp, layer 4 is broadened whereas the deeper layer 5a is accentuated (**black triangles**). In comparison, layer 2 is accentuated in Mop. Here the comparison across MRH and LSM is particularly informative. For details on structure and function of these regions see [10] for MOp and* [11] *for SSp. **Scale bar** is 5 mm.*

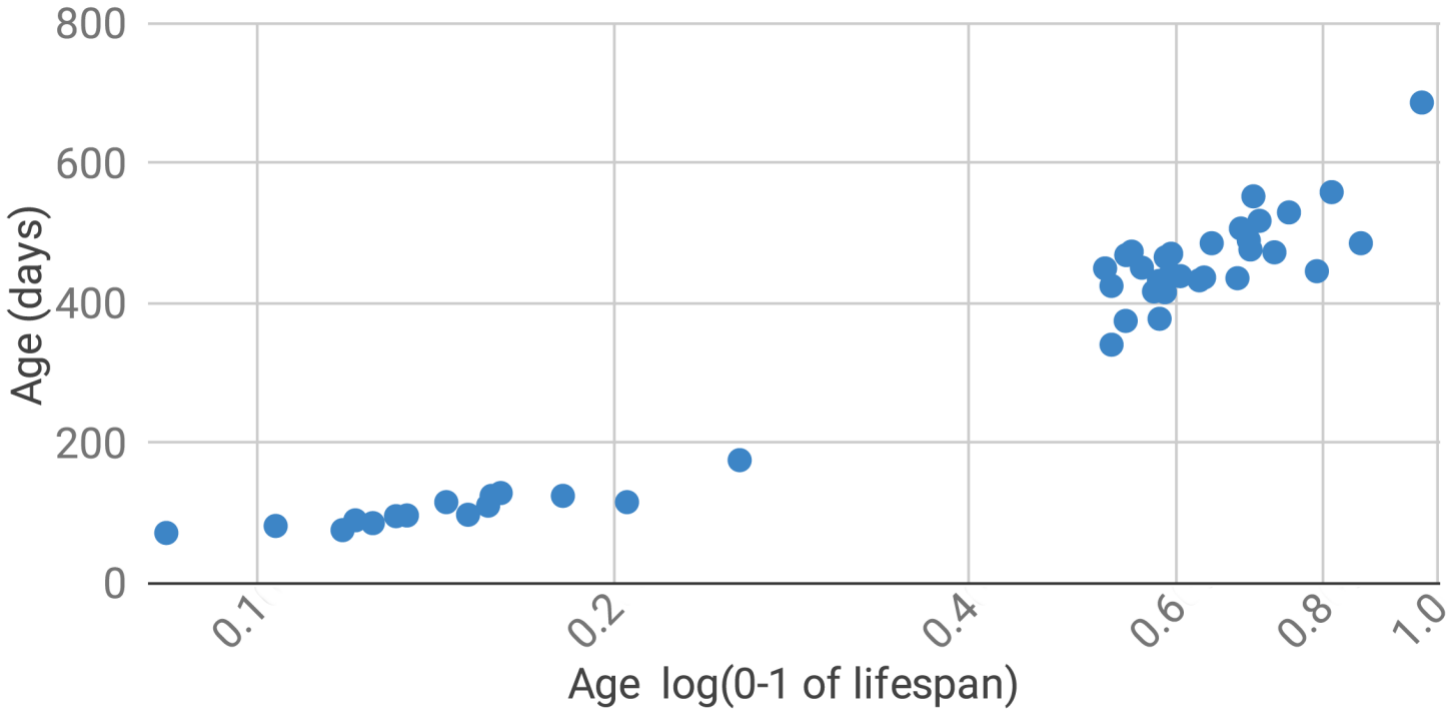

Figure S8 *Plot of age of animals in the hi throughput experiment (Experiment # 4) as a function of their lifespan showing clustering of 47 young animals (mean 102 days) and 64 old animals(mean 463 days)*

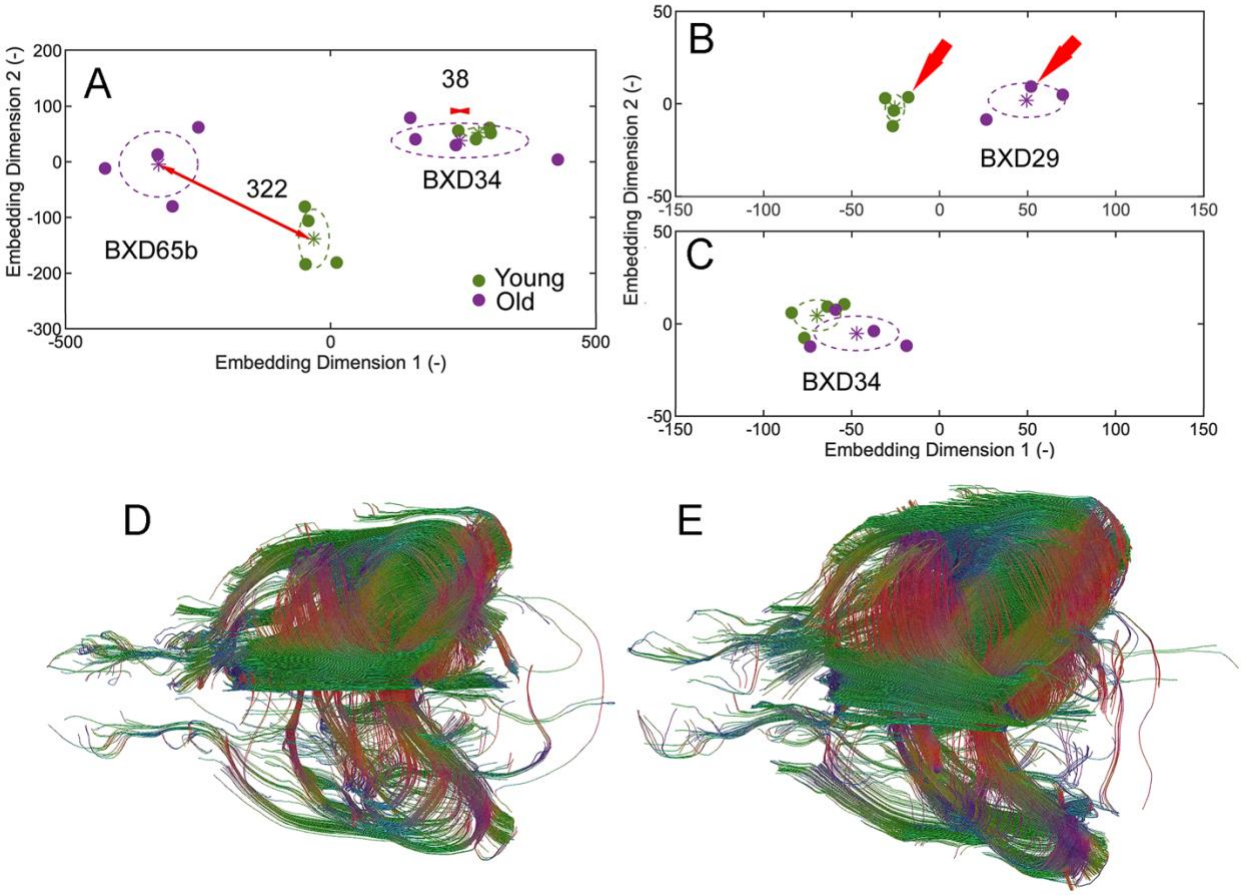

Figure S9 A) Analysis of connectivity changes with age identified the BXD65b as the strain with the greatest global change between young and old animals and the BXD34 as the strain with the least change. B) The subiculum was one region in which there was significant change in connectivity with age with the largest change in the BXD29. C) By comparison, the change in the subiculum connectivity was limited for the BXD34. D) Tractography generated by seeding the right subiculum in the young BXD29 (red arrow in B). E) Tractography generated from the connectomes of the old BXD29 specimens (red arrow in B). The greater number of streamlines in E vs D are a visual demonstration of the differences in the connectome. These are raw unfiltered tracts.

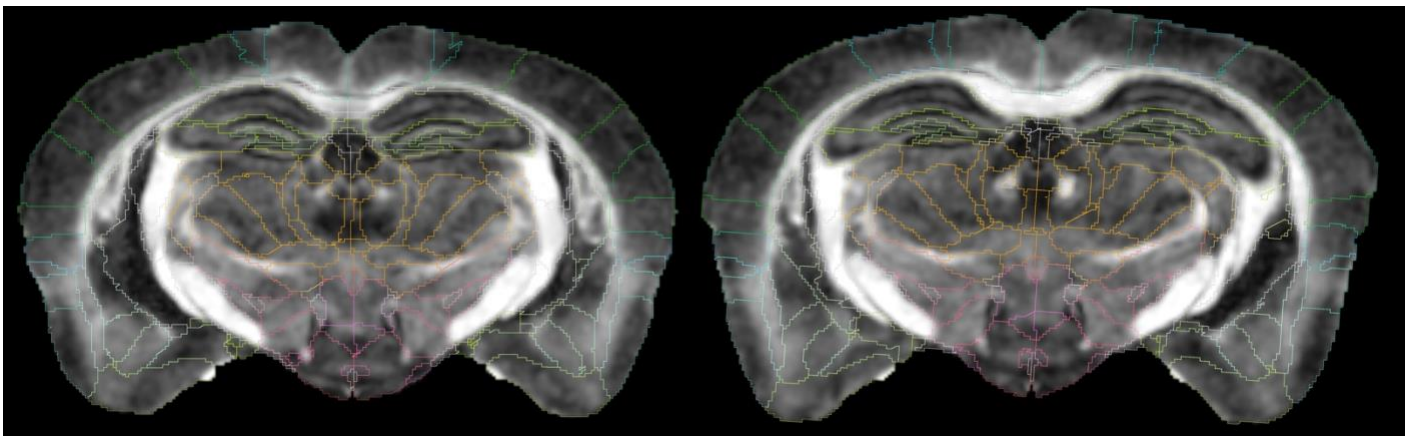

Figure S10. *Representative specimens from the study described in Figure S 9 showing reproducibility of the labeling in two of the old (418 days) BXD65b where there are age related differences. Labels have been superimposed to allow one to appreciate the robustness of the SAMBA pipeline.*

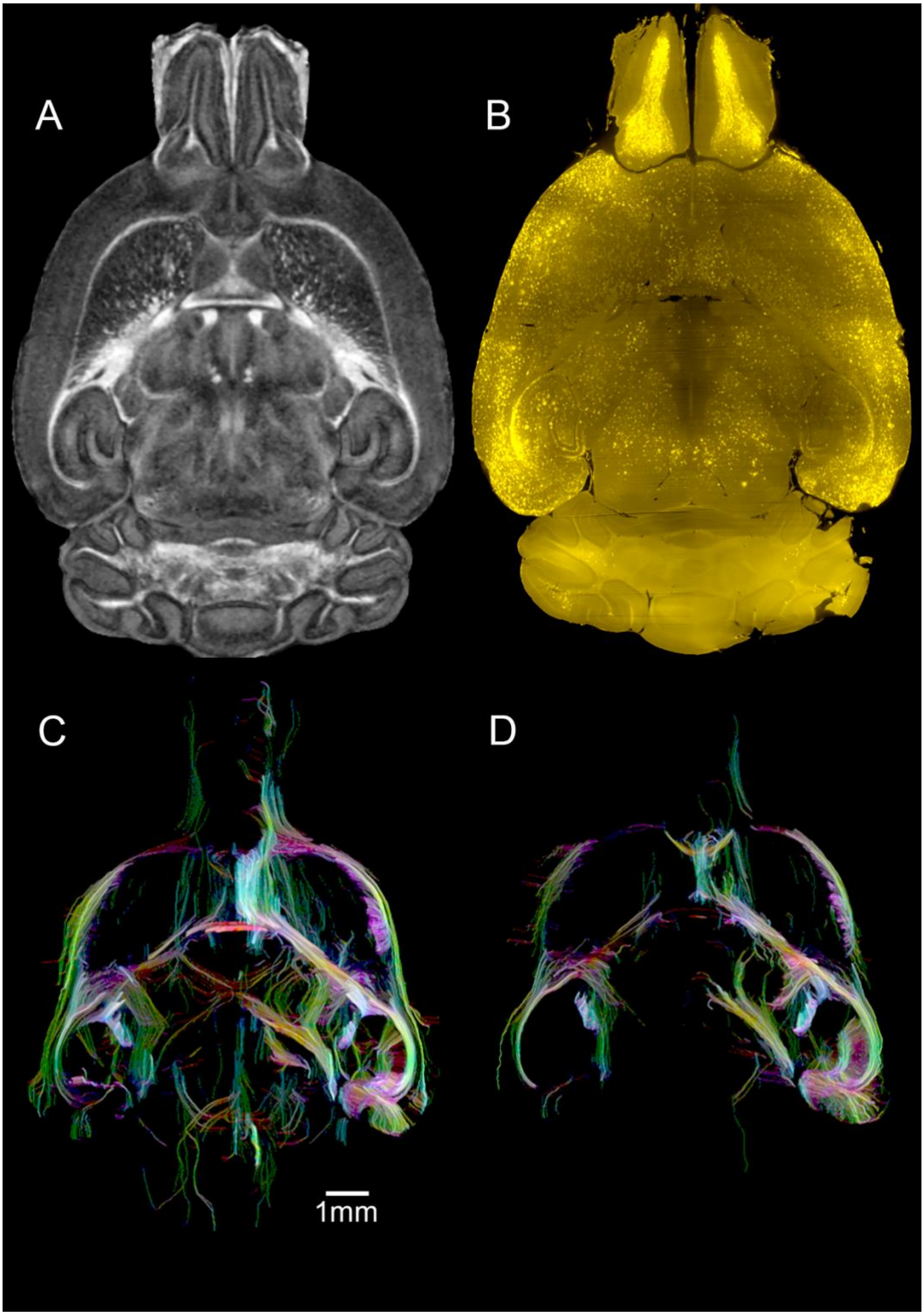

Figure S11 *Combined MRH/LSM images from ongoing Alzheimer's disease study of resilience in the 5XFADBXD model. A) Fractional anisotropy image from 14-month female 5XFADBXD77 animal acquired with high throughput protocol described in Figure S6. B) LSM image of the aβ LSM volume aligned with the FA image. C) Tractogram from seeding right subiculum in the 14-month female nTgBXD77 (control) specimen. D) Tractogram from seeding the right subiculum in the 5XFADBXD77.*

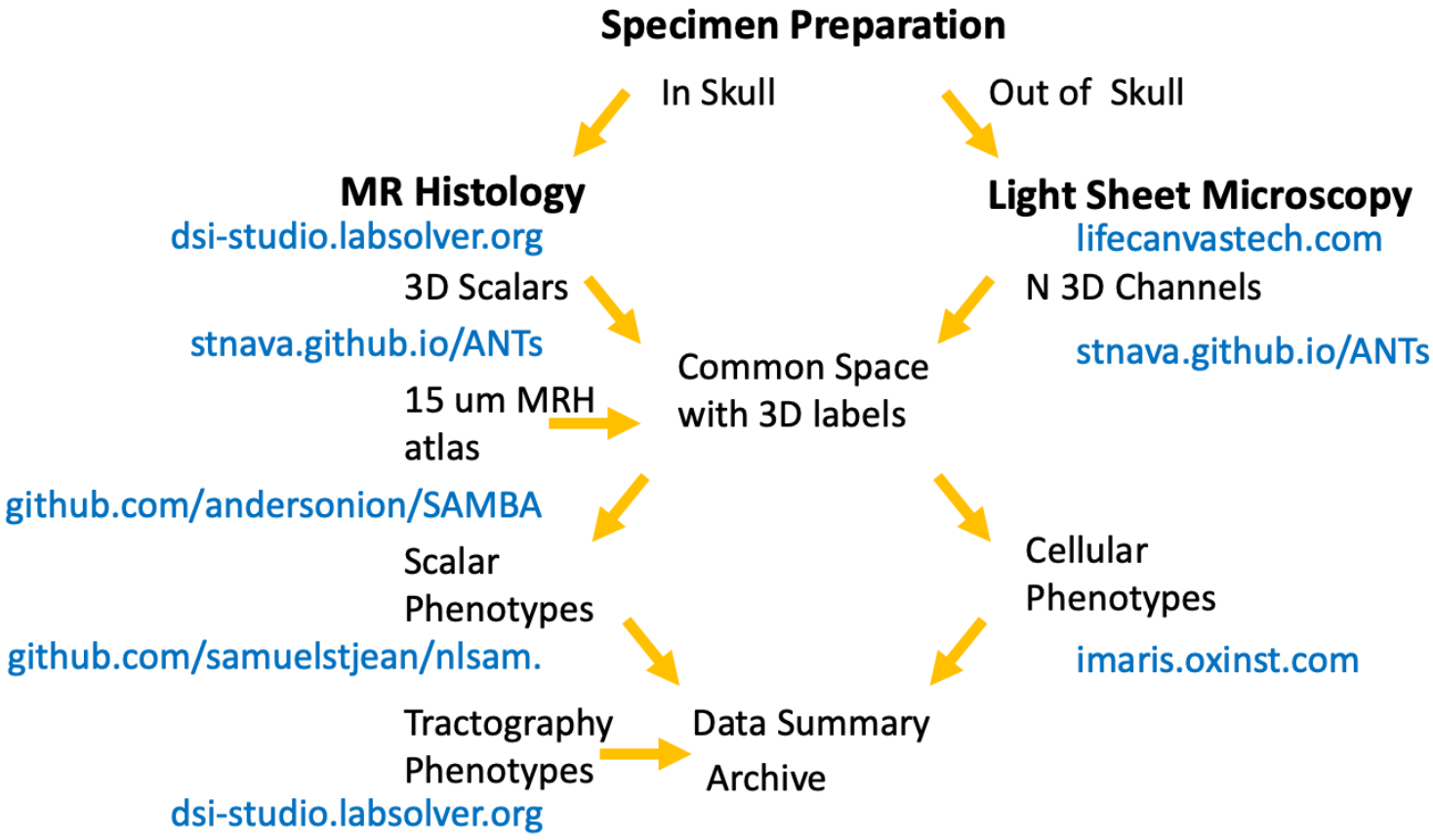

Figure S12. *Workflow for HiDIver. The actively stained brain (still in the cranium) is scanned in a 9.4T MRI system equipped with coils achieving gradients more than 100 times those of a clinical scanner. Compressed sensing is used to accelerate a high angular diffusion tensor acquisition. A series of image pipelines process the large (250 GB) 4D MRI data to derive scalar and tractography data. A new MR atlas acquired at 15* μm *isotropic resolution includes a subset of 360 labels from the Allen Brain Atlas Common Coordinate Framework. A second pipeline maps these labels onto the strain under study. The brain is removed from the skull, cleared (SHIELD), stained (SWITCH) and scanned with structured plane illumination microscopy @ 1.8 X1.8 x 4* μm. *A third pipeline registers the light sheet data to the common space defined by the MR histology image of the strain under study (in the skull) removing the distortions that accompany LSM. Image derived phenotypes from the 360 ROI are aggregated into a final summary. Black text describes the stage of the process. Yellow arrows show the workflow. Blue entries show the software and source.*

Detailed Methods

Data Acquisition. MRH images were acquired on a 9.4T/89 mm vertical bore magnet with an Agilent Direct Drive console (Vnmrj 4.0). A Resonance Research Model BRG-88_41 provided peak gradients up to 2500 mT/m. The brain was placed in a solenoid coil constructed from a single sheet of silver foil. Two imaging sequences were used; 1) a

multigradient echo (n = 4) sequence (TR/TE = 100/4.4 ms) and a Stesjkal/Tanner spin echo sequence for diffusion tensor imaging (DTI) (TR/TE = 100/12-19 ms) [12]. Both sequences employed phase encoding along the short axes of the specimen (x and y) with the readout gradient applied along the long axis of the specimen (z).

Compressed Sensing Reconstruction. Compressed sensing was used in both sequences [13] [14]. A probabilistic map was generated for sparse sampling along the two-phase encoding axes **(Figure S13)**. A script on the scanner automated acquisition and transfer to the cluster (**Figure S14**). A Fourier transform was applied along the z axis producing 256–2000 2D files which were distributed to multiple processors for iterative reconstruction. A baseline acquisition was included in every 10–15th volume to monitor drift in the spectrometer.

Label registration. Labels from the atlas were transferred to the volume under study using our SAMBA pipeline [29]. Stage 1, the affine transform, used the DWI with Mattes and a stringent convergence threshold (x 10^{-8}). Stage 2, the diffeomorphic transform used hybrid images. High contrast edges were extracted from the DWI and projected onto the FA using maximum intensity projection. The resulting hybrid has a value of 1 anywhere a significant edge was detected e.g. around ventricles where there is limited definition in the FA. The diffeomorphic registration used cross correlation. This transform was inverted to map the labels back to the specimen in the laboratory space. The pipeline calculated a coefficient of variation between left and right hemispheres as a quality assurance check. With few localized exceptions, the CNS of mice is bilaterally symmetric, and the CVs of left and right are expected to be under 0.04 for cases without any neuropathology. Wang and colleagues found that these mean CV values average about 0.015 with a corresponding error term (see their Figure S10) [15]. We use L-R CV values to highlight possible errors introduced by complex technical workflows. The summary of regional scalar phenotypes was written to a spreadsheet with metadata [31].

Tractography and connectome generation. Tractography, track density images (TDI) and connectomes were generated in DSI Studio using the generalized q-sampling imaging (GQI) algorithm with multiple fibers (up to 4) in each voxel [16, 17]. Connectomes were generated using the labels from the label registration pipeline. Track density images were generated using a super sampling algorithm described by Calamante et al. [18, 19]. Images in these previous studies were acquired with 100 µm spatial resolution and 30 angles—a resolution index of ~3.0×10^4 [20]. The resolution index achieved here is 3.2×10^7, about three orders of magnitude higher than previous work. Whole brain tractography was acquired by seeding the 4D volume 54 million points. Step size was set to 0.75 µm at a QA threshold of 0.1% of the peak QA histogram generating track density images with nominal sampling of 5 µm.

LSM registration. The brain was extracted from the skull and shipped to LifeCanvas Technologies (Cambridge MA) where commercial protocols for clearing, immunohistochemistry and scanning were executed (Supplement). For each specimen three LSM volumes were acquired. The NeuN was registered to the DWI for the atlas creation and aging comparisons [21]. The autofluorescence images were registered to the DWI for the tractography comparisons. In step 1, the LSM volume was down sampled to the resolution of the MRH volume (15 μm or 25 μm). A pipeline built on ANTs executed the registration in three stages: 1) Affine transformation using mutual information; 2) B spline using cross correlation; 3) Diffeomorphic transform using mutual information. The transform from the low resolution (15 or 25 μm) arrays was then applied to the full resolution LSM images. Images were examined in registration with MRH in Imaris (Oxford Instruments).

Light Sheet Acquisition Paraformaldehyde-fixed samples were preserved using SHIELD reagents (LifeCanvas Technologies) using the manufacturer's instructions [22]- each brain was incubated in 20mL of SHIELD-off solution for 4 d followed by 1 d of incubation in 20mL SHIELD-on solution. The meninges then were removed from each sample. Samples were incubated in Clearing Buffer A (LifeCanvas Technologies) overnight then actively delipidated using a LifeCanvas Technologies SmartClear II Pro device for 6 days using stochastic electrotransport [23] .After depilation the samples were washed in PBS with 0.1% Tween20 for 1 d to remove SDS. For immunolabeling the samples were incubated in SmartLabel Primary Sample Buffer (LifeCanvas Technologies) overnight with an additional 5-6 h incubation with fresh buffer before primary immunolabeling in a SmartLabel device employing eFLASH [24]technology which integrates stochastic electrotransport [23] and SWITCH [25] for 14 h. The samples were then washed in PBS for 7-8h before overnight fixation in 4% paraformaldehyde followed by incubation in secondary labeling buffer at 37 C with two refreshes over the course of 7-8h before secondary labeling in the SmartLabel device. For each brain, 10 μg of rabbit anti-Iba1 (Cell Signaling Technologies 17198S*) primary antibody, 10 μg mouse anti-NeuN (Encor MCA-1B7), 6 μg rabbit anti-NeuN (Cell Signaling Technologies 24307S*), or 20 μg mouse anti-MBP (Encor MCA-7G7). Secondary antibodies were used at a 2:1 Secondary:Primary molar ratio. After immunolabeling, samples were incubated in 50% EasyIndex (RI = 1.52, LifeCanvas Technologies) overnight at 37 C followed by 1 d incubation in 100% EasyIndex for refractive index matching. After index matching the samples were imaged using a SmartSPIM axially swept light sheet microscope using a 3.6x (0.2 NA) (LifeCanvas Technologies). The smart SPIM light sheet fluorescence microscope provides whole brain coverage (3650 μm field of view) at 1.8 x 1.8 x 4.0 μm with a 3.6X objective producing three stacks of registered 2D .tiff images—one stack for each excitation wavelength. Typical array size for a stack is 7600 x 10600 x 2250 or about 250 GB.

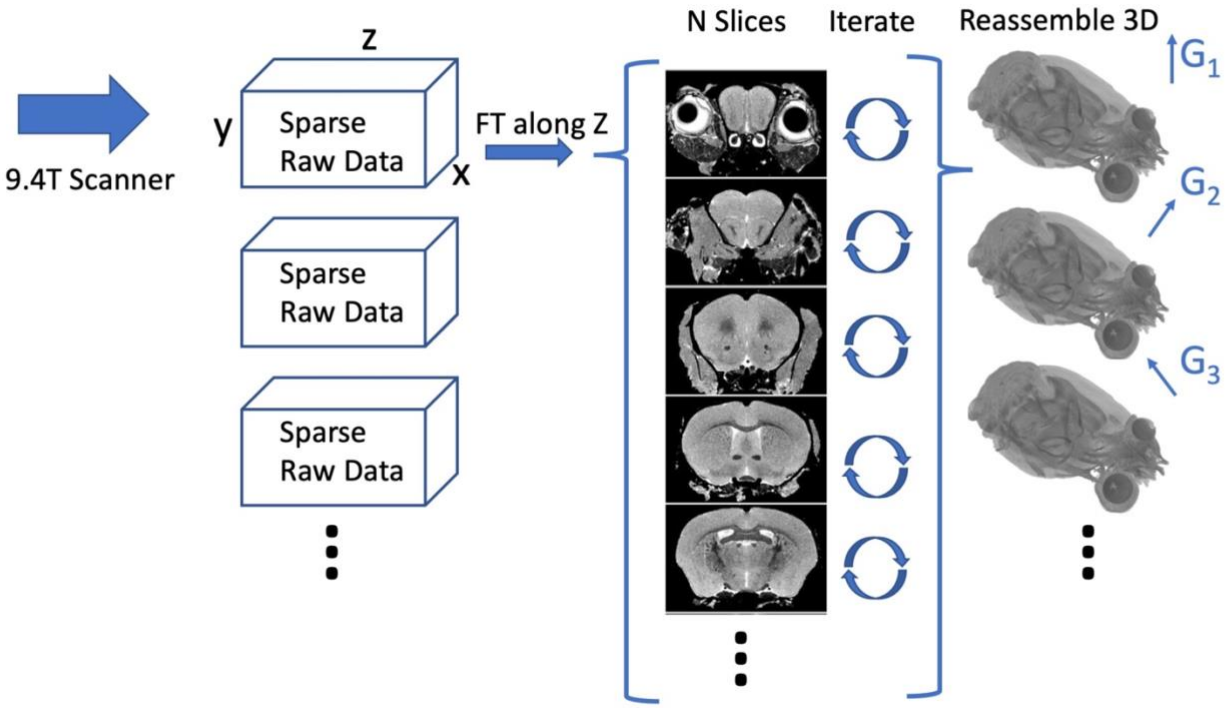

Figure S13 *A pipeline integrates a 4-dimensional acquisition from the scanner with compressed sensing reconstruction in a high-performance Dell cluster. Data from the scanner is streamed from the scanner to the cluster. Fourier space is under sampled by a factor of 8 using a probabilistic distribution along two (phase) dimensions of acquisition. A Fourier transform along the fully sampled readout axis produces up to 2000 2 dimensional arrays which are launched as individual iterative reconstructions in the cluster. Upon completion of the iterative reconstruction, these 2D arrays are reassembled into a 3D volume. A script on the scanner launches the next scan.*

Computer Resources. Scaling MRH to the higher resolution reported here requires high-performance computer systems (**Figure S14**) that can handle multiple 3D arrays as large as 1 TB. In our implementation, source image files were streamed to a 604-core 18-node cluster for automated reconstruction, data reduction, and alignment. We relied on two servers with 1.5 TB of memory that enable interactive analysis of HiDiver data using Fiji (https://fiji.sc/), Slicer (https://www.slicer.org/), and Imaris (https://imaris.oxinst.com). Large (100 TB) high performance RAIDs provided local storage to facilitate remote interactive analysis via Citrix.

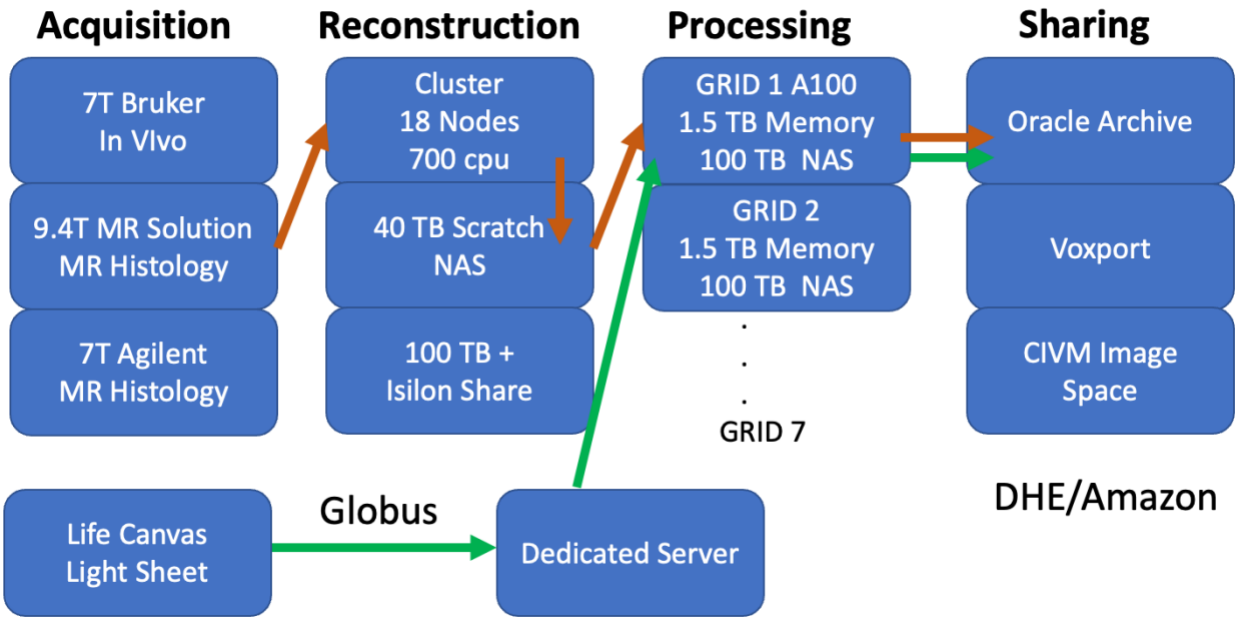

Figure S14. *High performance computer infrastructure to facilitate combined MRH and LSM with large multidimensional images. Key is the division of the workflow into 4 stages—acquisition, reconstruction, post-processing, and sharing with computational resources optimized for large data files at each stage. The brown arrows show the flow of MRH data. The green arrows show the flow of LSM data. DHE-Duke Health Enterprise network hosting the Oracle archive. CIVM Image Space- dedicated image sharing application on an Amazon EC2/S3 allowing review and download of very large data sets.*

ROI#	Name	Acronym	CCF3 Structures Combined
1	Cerebrum	CH	
2	Basic cell groups and regions	grey	
3	Olfactory bulb	OB	AOB, AON, MOB
4	Anterior olfactory nucleus	AON	
5	Frontal pole, cerebral cortex	FRP	
6	Orbital area	ORB	
7	Prelimbic area	PL	
8	Infralimbic area	ILA	
9	Anterior cingulate area	ACA	
10	Agranular insular area	AI	
11	Gustatory areas	GU	
12	Piriform area	PIR	
13	Visceral area	VISC	

14	Primary motor area	MOp	
15	Secondary motor area	MOs	
16	Primary somatosensory area	SSp	
17	Primary somatosensory area, barrel field	SSp-bfd	
18	Supplemental somatosensory area	SSs	
19	Posterior parietal association areas	PTLp	
20	Auditory areas	AUD	
21	Temporal association areas	TEa	
22	Ectorhinal area	ECT	
23	Perirhinal area	PERI	
24	Retrosplenial area	RSP	
25	Visual areas	VIS	
26	Primary visual area	VISp	
27	Entorhinal area	ENT	
28	Subicular region	SUBR	SUB, PRE, POST, PAR, ProS
29	Hippocampus	HI	CA, DG
30	Hippocampal region	HIP	
31	Field CA1	CA1	
32	Field CA3	CA3	
33	Dentate gyrus	DG	
34	Dentate gyrus, granule cell layer	DG-sg	
35	Dentate gyrus, polymorph layer	DG-po	
36	Claustrum	CLA	
37	Central amygdalar nucleus	CEA	
38	Striatum-like amygdalar nuclei	sAMY	
39	Medial amygdalar nucleus	MEA	
40	Lateral amygdalar nucleus	LA	
41	Basolateral amygdalar nucleus	BLA	
42	Basomedial amygdalar nucleus	BMA	
43	Posterior amygdalar nucleus	PA	
44	Cortical amygdalar zones	COAz	COA, PAA, TR
45	Endopiriform nucleus	EP	
46	Striatum	STR	
47	Striatum dorsal region	STRd	
48	Nucleus accumbens	ACB	
49	Fundus of striatum	FS	
50	Olfactory tubercle	OT	
51	Globus pallidus, external segment	GPe	
52	Globus pallidus, internal segment	GPi	
53	Substantia innominata	SI	
54	Medial septal complex	MSC	
55	Lateral septal nucleus	LS	
56	Bed nuclei of the stria terminalis	BST	

57	Magnocellular nucleus _Meynert_	MA
58	Thalamus	TH
59	Anteromedial nucleus	AM
60	Anterodorsal nucleus	AD
61	Anteroventral nucleus of thalamus	AV
62	Lateral dorsal nucleus of the thalamus	LD
63	Ventral anterior-lateral complex of the thalamus	VAL
64	Ventral medial nucleus of the thalamus	VM
65	Ventral posterior complex of the thalamus	VP
66	Ventral posteromedial nucleus of the thalamus	VPM
67	Ventral posterolateral nucleus of the thalamus	VPL
68	Parataenial nucleus	PT
69	Paraventricular nucleus of the thalamus	PVT
70	Nucleus of reuniens	RE
71	Central lateral nucleus of the thalamus	CL
72	Central medial nucleus of the thalamus	CM
73	Paracentral nucleus	PCN
74	Parafascicular nucleus	PF
75	Posterior intralaminar thalamic nucleus	PIL
76	Mediodorsal nucleus of thalamus	MD
77	Lateral posterior nucleus of the thalamus	LP
78	Posterior complex of the thalamus	PO
79	Medial geniculate complex, dorsal part	MGd
80	Medial geniculate complex, ventral part	MGv
81	Medial geniculate complex, medial part	MGm
82	Dorsal part of the lateral geniculate complex	LGd
83	Ventral part of the lateral geniculate complex	LGv
84	Reticular nucleus of the thalamus	RT
85	Lateral habenula	LH
86	Medial habenula	MH
87	Hypothalamus	HY
88	Medial preoptic nucleus	MPN
89	Anterior hypothalamic nucleus	AHN
90	Ventromedial hypothalamic nucleus	VMH
91	Posterior hypothalamic nucleus	PH
92	Mammillary body	MBO
93	Suprachiasmatic nucleus	SCH
94	Arcuate hypothalamic nucleus	ARH
95	Paraventricular hypothalamic nucleus	PVH
96	Lateral preoptic area	LPO
97	Tuberal nucleus	TU
98	Lateral hypothalamic area	LHA

99	Subthalamic nucleus	STN	
100	Zona incerta	ZI	
101	Superior colliculus, sensory related	SCs	
102	Superior colliculus, motor related	SCm	
103	Inferior colliculus	IC	
104	Inferior colliculus, central nucleus	ICc	
105	Parabigeminal nucleus	PBG	
106	Pedunculopontine nucleus	PPN	
107	Pretectal region	PRT	
108	Oculomotor region	IIIR	III, EW
109	Periaqueductal gray	PAG	
110	Red nucleus	RN	
111	Midbrain reticular nucleus	MRN	
112	Cuneiform nucleus	CUN	
113	Interpeduncular nucleus	IPN	
114	Ventral tegmental area	VTA	
115	Substantia nigra, compact part	SNc	
116	Substantia nigra, reticular part	SNr	
117	Dorsal nucleus raphe	DR	
118	Pons	P	
119	Nucleus of the lateral lemniscus	NLL	
120	Superior olivary complex	SOC	
121	Parabrachial nucleus	PB	
122	Principal sensory nucleus of the trigeminal	PSV	
123	Pontine central gray	PCG	
124	Pontine gray	PG	
125	Trigeminal motor complex	VMc	V, P5, I5, Acs5
126	Facial motor nucleus	VII	
127	Dorsal tegmental nucleus	DTN	
128	Laterodorsal tegmental nucleus	LDT	
129	Tegmental reticular nucleus	TRN	
130	Pontine reticular formation	PRF	PRNc, PRNr
131	Raphe ventral complex	RVC	IF, IPN, RL, CLI, CS
132	Hemispheric regions	HEM	
133	Vermal regions	VERM	
134	Paraflocculus	PFL	
135	Floccular nodular region	FLNOD	NOD, FL, UVU
136	Dentate nucleus	DN	
137	Interposed nucleus	IP	
138	Fastigial nucleus	FN	
139	Vestibulocerebellar nucleus	VeCB	
140	Nucleus of the trapezoid body	NTB	
141	Spinal nucleus of the trigeminal region	SPVr	SPVC, SPVI, SPVO

142	Nucleus of the solitary tract	NTS	
143	Dorsal cochlear nucleus	DCO	
144	Ventral cochlear nucleus	VCO	
145	Vestibular nuclei	VNC	
146	Spinal vestibular nucleus	SPIV	
147	Dorsal column nuclei	DCN	
148	Inferior olivary complex	IO	
149	Perihypoglossal nuclei	PHY	
150	Dorsal motor nucleus of the vagus nerve	DMX	
151	Hypoglossal nucleus	XII	
152	Medullary reticular zone	MRz	GRN, LRN, MARN, MDRN, PARN, PGRN,
153	Intermediate reticular nucleus	IRN	
154	Medulla, raphe, behavioral state related	MY-sat	
155	fiber tracts	fiber tracts	
156	corpus callosum	cc	ccb, ccg, ccs, fp
157	cingulum bundle	cing	
158	anterior commissure	ac	act, aco
159	optic tract and chiasm	optc	opt,och
160	dorsal hippocampal commissure	dhc	
161	fimbria	fi	
162	columns of the fornix	fx	
163	stria terminalis	st	
164	thalamus related	lfbst	
165	medial forebrain bundle	mfb	
166	fasciculus retroflexus	fr	
167	posterior commissure	pc	
168	corticospinal tract	cst	
169	medial lemniscus	ml	
170	lateral lemniscus	ll	
171	medial longitudinal fascicle	mlf	
172	superior cerebelar peduncles	scp	
173	inferior cerebellar peduncle	icp	
174	trigeminal nerve	Vn	
175	cochlear nerve	cVIIIn	
176	lateral ventricle	VL	
177	third ventricle	V3	
178	fourth ventricle	V4	
179	cerebral aqueduct	AQ	
180	Whole brain _root_	Brain	
1001	Cerebrum	CH	
1002	Basic cell groups and regions	grey	
1003	Olfactory bulb	OB	AOB, AON, MOB

1004	Anterior olfactory nucleus	AON	
1005	Frontal pole, cerebral cortex	FRP	
1006	Orbital area	ORB	
1007	Prelimbic area	PL	
1008	Infralimbic area	ILA	
1009	Anterior cingulate area	ACA	
1010	Agranular insular area	AI	
1011	Gustatory areas	GU	
1012	Piriform area	PIR	
1013	Visceral area	VISC	
1014	Primary motor area	MOp	
1015	Secondary motor area	MOs	
1016	Primary somatosensory area	SSp	
1017	Primary somatosensory area, barrel field	SSp-bfd	
1018	Supplemental somatosensory area	SSs	
1019	Posterior parietal association areas	PTLp	
1020	Auditory areas	AUD	
1021	Temporal association areas	TEa	
1022	Ectorhinal area	ECT	
1023	Perirhinal area	PERI	
1024	Retrosplenial area	RSP	
1025	Visual areas	VIS	
1026	Primary visual area	VISp	
1027	Entorhinal area	ENT	
1028	Subicular region	SUBR	SUB, PRE, POST, PAR, ProS
1029	Hippocampus	HI	CA, DG
1030	Hippocampal region	CA3	
1031	Field CA1	CA1	
1032	Field CA3	CA3	
1033	Dentate gyrus	DG	
1034	Dentate gyrus, granule cell layer	DG-sg	
1035	Dentate gyrus, polymorph layer	DG-po	
1036	Claustrum	CLA	
1037	Central amygdalar nucleus	CEA	
1038	Striatum-like amygdalar nuclei	sAMY	
1039	Medial amygdalar nucleus	MEA	
1040	Lateral amygdalar nucleus	LA	
1041	Basolateral amygdalar nucleus	BLA	
1042	Basomedial amygdalar nucleus	BMA	
1043	Posterior amygdalar nucleus	PA	
1044	Cortical amygdalar zones	COAz	COA, PAA, TR
1045	Endopiriform nucleus	EP	
1046	Striatum	STR	

1047	Striatum dorsal region	STRd
1048	Nucleus accumbens	ACB
1049	Fundus of striatum	FS
1050	Olfactory tubercle	OT
1051	Globus pallidus, external segment	GPe
1052	Globus pallidus, internal segment	GPi
1053	Substantia innominata	SI
1054	Medial septal complex	MSC
1055	Lateral septal nucleus	LS
1056	Bed nuclei of the stria terminalis	BST
1057	Magnocellular nucleus _Meynert_	MA
1058	Thalamus	TH
1059	Anteromedial nucleus	AM
1060	Anterodorsal nucleus	AD
1061	Anteroventral nucleus of thalamus	AV
1062	Lateral dorsal nucleus of the thalamus	LD
1063	Ventral anterior-lateral complex of the thalamus	VAL
1064	Ventral medial nucleus of the thalamus	VM
1065	Ventral posterior complex of the thalamus	VP
1066	Ventral posteromedial nucleus of the thalamus	VPM
1067	Ventral posterolateral nucleus of the thalamus	VPL
1068	Parataenial nucleus	PT
1069	Paraventricular nucleus of the thalamus	PVT
1070	Nucleus of reuniens	RE
1071	Central lateral nucleus of the thalamus	CL
1072	Central medial nucleus of the thalamus	CM
1073	Paracentral nucleus	PCN
1074	Parafascicular nucleus	PF
1075	Posterior intralaminar thalamic nucleus	PIL
1076	Mediodorsal nucleus of thalamus	MD
1077	Lateral posterior nucleus of the thalamus	LP
1078	Posterior complex of the thalamus	PO
1079	Medial geniculate complex, dorsal part	MGd
1080	Medial geniculate complex, ventral part	MGv
1081	Medial geniculate complex, medial part	MGm
1082	Dorsal part of the lateral geniculate complex	LGd
1083	Ventral part of the lateral geniculate complex	LGv
1084	Reticular nucleus of the thalamus	RT
1085	Lateral habenula	LH
1086	Medial habenula	MH
1087	Hypothalamus	HY
1088	Medial preoptic nucleus	MPN

1089	Anterior hypothalamic nucleus	AHN	
1090	Ventromedial hypothalamic nucleus	VMH	
1091	Posterior hypothalamic nucleus	PH	
1092	Mammillary body	MBO	
1093	Suprachiasmatic nucleus	SCH	
1094	Arcuate hypothalamic nucleus	ARH	
1095	Paraventricular hypothalamic nucleus	PVH	
1096	Lateral preoptic area	LPO	
1097	Tuberal nucleus	TU	
1098	Lateral hypothalamic area	LHA	
1099	Subthalamic nucleus	STN	
1100	Zona incerta	ZI	
1101	Superior colliculus, sensory related	SCs	
1102	Superior colliculus, motor related	SCm	
1103	Inferior colliculus	IC	
1104	Inferior colliculus, central nucleus	ICc	
1105	Parabigeminal nucleus	PBG	
1106	Pedunculopontine nucleus	PPN	
1107	Pretectal region	PRT	
1108	Oculomotor region	IIIR	III, EW
1109	Periaqueductal gray	PAG	
1110	Red nucleus	RN	
1111	Midbrain reticular nucleus	MRN	
1112	Cuneiform nucleus	CUN	
1113	Interpeduncular nucleus	IPN	
1114	Ventral tegmental area	VTA	
1115	Substantia nigra, compact part	SNc	
1116	Substantia nigra, reticular part	SNr	
1117	Dorsal nucleus raphe	DR	
1118	Pons	P	
1119	Nucleus of the lateral lemniscus	NLL	
1120	Superior olivary complex	SOC	
1121	Parabrachial nucleus	PB	
1122	Principal sensory nucleus of the trigeminal	PSV	
1123	Pontine central gray	PCG	
1124	Pontine gray	PG	
1125	Trigeminal motor complex	VMc	V, P5, I5, Acs5
1126	Facial motor nucleus	VII	
1127	Dorsal tegmental nucleus	DTN	
1128	Laterodorsal tegmental nucleus	LDT	
1129	Tegmental reticular nucleus	TRN	
1130	Pontine reticular formation	PRF	PRNc, PRNr
1131	Raphe ventral complex	RVC	IF, IPN, RL, CLI, CS

1132	Hemispheric regions	HEM	
1133	Vermal regions	VERM	
1134	Paraflocculus	PFL	
1135	Floccular nodular region	FLNOD	NOD, FL, UVU
1136	Dentate nucleus	DN	
1137	Interposed nucleus	IP	
1138	Fastigial nucleus	FN	
1139	Vestibulocerebellar nucleus	VeCB	
1140	Nucleus of the trapezoid body	NTB	
1141	Spinal nucleus of the trigeminal region	SPVr	SPVC, SPVI, SPVO
1142	Nucleus of the solitary tract	NTS	
1143	Dorsal cochlear nucleus	DCO	
1144	Ventral cochlear nucleus	VCO	
1145	Vestibular nuclei	VNC	
1146	Spinal vestibular nucleus	SPIV	
1147	Dorsal column nuclei	DCN	
1148	Inferior olivary complex	IO	
1149	Perihypoglossal nuclei	PHY	
1150	Dorsal motor nucleus of the vagus nerve	DMX	
1151	Hypoglossal nucleus	XII	
1152	Medullary reticular zone	MRz	GRN, LRN, MARN, MDRN, PARN, PGRN,
1153	Intermediate reticular nucleus	IRN	
1154	Medulla, raphe, behavioral state related	MY-sat	
1155	fiber tracts	fiber tracts	
1156	corpus callosum	cc	ccb, ccg, ccs, fp
1157	cingulum bundle	cing	
1158	anterior commissure	ac	act, aco
1159	optic tract and chiasm	optc	opt,och
1160	dorsal hippocampal commissure	dhc	
1161	fimbria	fi	
1162	columns of the fornix	fx	
1163	stria terminalis	st	
1164	thalamus related	lfbst	
1165	medial forebrain bundle	mfb	
1166	fasciculus retroflexus	fr	
1167	posterior commissure	pc	
1168	corticospinal tract	cst	
1169	medial lemniscus	ml	
1170	lateral lemniscus	ll	
1171	medial longitudinal fascicle	mlf	
1172	superior cerebelar peduncles	scp	
1173	inferior cerebellar peduncle	icp	

1174	trigeminal nerve	Vn
1175	cochlear nerve	cVIIIn
1176	lateral ventricle	VL
1177	third ventricle	V3
1178	fourth ventricle	V4
1179	cerebral aqueduct	AQ
1180	Whole brain _root_	Brain

Table S3. *Regions of interest for left hemisphere (ROI 1-180) and right hemisphere (ROI 1001-1180) for reduced CCFv3 (i.e. r1CCFv3 label set).*

Supplemental Figures and Tables References

1. Johnson, G.A. and L.W. Hedlund, *Three-dimensional morphology by magnetic resonance imaging*, U.P. Office, Editor. 2000, Duke University: U.S.A.
2. Johnson, G.A., et al., *Morphologic phenotyping with magnetic resonance microscopy: the visible mouse.* Radiology, 2002. **222**(3): p. 789-793.
3. Badea, A., A.A. Ali-Sharief, and G.A. Johnson, *Morphometric analysis of the C57BL/6J mouse brain.* Neuroimage, 2007. **37**(3): p. 683-93.
4. Avants, B.B., Tustison, N.J., Wu, J., Cook, P.A., Gee, J.C., , *An open source multivariate framework for n-tissue segmentation with evaluation on public data. .* Neuroinformatics, 2011. **9**: p. 381-400.
5. Anderson, R.J., et al., *Small Animal Multivariate Brain Analysis (SAMBA) – a High Throughput Pipeline with a Validation Framework.* Neuroinformatics, 2019. **17**: p. 451-472.
6. Basser, P.J., J. Mattiello, and D. LeBihan, *MR diffusion tensor spectroscopy and imaging.* Biophys J, 1994. **66**(1): p. 259-67.
7. Wang, Q., Ding,SL,Li,Y et al *The Allen Mouse Brain Common Coordinate Framework: A 3D Reference Atlas.* Cell, 2020. **181**: p. 936-953.
8. Li, C.X., et al., *Genetic analysis of barrel field size in the first somatosensory area (SI) in inbred and recombinant inbred strains of mice.* Somatosens Mot Res, 2005. **22**(3): p. 141-50.
9. St-Jean, S., Coupe,P, Descoteaux,M, Medical image Analysis, 2016. **32**: p. 115-130.
10. Muñoz-Castañeda, R., et al., *Cellular anatomy of the mouse primary motor cortex.* Nature, 2021. **598**(7879): p. 159-166.
11. Adibi, M., *Whisker-Mediated Touch System in Rodents: From Neuron to Behavior.* Front Syst Neurosci, 2019. **13**: p. 40.
12. Stejskal, E.O. and J.E. Tanner, *Spin diffusion measurements: spin echoes in the presence of a time-dependent field gradient.* Journal of Chemical Physics, 1963. **42**(1).
13. Lustig, M., Donoho,D, Pauly,JM, *Sparse MRI: The Application of Compressed Sensing for Rapid MR Imaging.* Magn Reson Medi, 2007. **58**: p. 1182-1195.
14. Wang, N., et al., *Whole mouse brain structural connectomics using magnetic resonance histology.* Brain Structure and Function, 2018. **223**(9): p. 4323-4335.
15. Wang N, A.R., Ashbrook DG, Gopalakrishnan V, Park Y, Priebe CE, Laoprasert R, Vogelstein JT, Williams RW, Johnson GA, *Variability and Heritability of Mouse Brain Structure: Microscopic MRI Atlases and Connectomes for Diverse Strains.* NeuroImage, 2020. **222**.
16. Yeh, F.-C., et al., *Deterministic Diffusion Fiber Tracking Improved by Quantitative Anisotropy.* PLoS ONE, 2013. **8**(11): p. e80713.

17. Yeh, F.-C., V.J. Wedeen, and W.-Y.I. Tseng, *Generalized q-Sampling Imaging.* IEEE Transactions on Medical Imaging, 2010. **29**(9): p. 1626-1635.
18. Calamante, F., Tournier,JD,Jackson, GD, Connelly A, *Track-density imaging (TDI): Super-resolution white matter imaging using whole-brain track-density mapping.* NeuroImage, 2010. **53**(4).
19. Calamante, F., et al., *Super-resolution track-density imaging studies of mouse brain: Comparison to histology.* NeuroImage, 2012. **59**(1): p. 286-296.
20. Johnson, G.A., Wang, N, Anderson,R.J., Chen,M., Cofer,G.P., Gee, J.C., Pratson, F., Tustison,N., White, L.E. , *Whole mouse brain connectomics.* J Comp Neurol., 2018. **12**: p. 1-12.
21. Tian Y, C.J., Johnson GA, *Restoring morphology of light sheet microscopy data based on magnetic resonance histology.* Frontiers in Neuroscience, 2023. **16**(16:1011895.).
22. Park, Y.-G., et al., *Protection of tissue physicochemical properties using polyfunctional crosslinkers.* Nature Biotechnology, 2018. **37**(1): p. 73-83.
23. Kim, S.Y., et al., *Stochastic electrotransport selectively enhances the transport of highly electromobile molecules.* Proc Natl Acad Sci U S A, 2015. **112**(46): p. E6274-83.
24. Yun DH, e.a., *Ultrafast immunostaining of organ-scale tissues for scalable proteomic phenotyping.* BioRxiv, 2019.
25. Murray, E., et al., *Simple, Scalable Proteomic Imaging for High- Dimensional Profiling of Intact Systems.* Cell, 2015. **163**(6): p. 1500-1514.